AIAA JOURNAL
Vol. 47, No. 11, November 2009

# Numerical Analysis of Film Cooling in Advanced Rocket Nozzles

Emanuele Martelli,* Francesco Nasuti,† and Marcello Onofri‡
*University of Rome "La Sapienza," 00184 Rome, Italy*

DOI: 10.2514/1.39217

**The key demand on future space transportation systems is the concurrent reduction of Earth-to-orbit launch costs and increase of launcher reliability and operational efficiency. A common way of slightly improving performance of gas-generator open-cycle engines is the injection of the turbine exhaust gas into the nozzle divergent section, which is also used for wall film cooling. The present study focuses on a numerical parametric analysis of the film-cooling efficiency in dual-bell nozzles. The secondary gas injection is made in the first bell, and it is found that the expansion fan originating from the inflection helps the film to better protect the wall. The results of fully-attached-flow simulations are also used to study the influence of film cooling on the expected behavior of nozzle side loads during operation with separated flow in the second bell.**

## Nomenclature

| | | |
|---|---|---|
| $A$ | = | cross-sectional area |
| $a$ | = | speed of sound |
| $c_p$ | = | constant-pressure specific heat |
| $g$ | = | gravity constant |
| $l$ | = | length |
| $M$ | = | Mach number |
| $\dot{m}$ | = | mass flow rate |
| $p$ | = | pressure |
| $R$ | = | gas constant |
| $Re$ | = | Reynolds number |
| $r$ | = | radius |
| $s$ | = | slot height |
| $T$ | = | temperature |
| $u$ | = | flow velocity |
| $V$ | = | flight velocity |
| $x$ | = | abscissa |
| $\alpha$ | = | change of wall angle at inflection |
| $\beta$ | = | blowing ratio, $(\rho u)_f/(\rho u)_m$ |
| $\epsilon$ | = | area ratio, $A/A_t$ |
| $\eta$ | = | film-cooling effectiveness |
| $\lambda$ | = | nondimensional axial distance from inflection, $l/r_t$ |
| $\mu$ | = | viscosity |
| $\xi$ | = | nondimensional abscissa, $x/r_t$ |
| $\pi$ | = | nondimensional pressure, $p/p_c$ |
| $\pi_\xi$ | = | nondimensional wall pressure gradient, $\mathrm{d}\pi/\mathrm{d}\xi$ |
| $\rho$ | = | density |
| $\sigma$ | = | nondimensional slot height, $s/r_t$ |
| $\tau_{\mathrm{sl}}$ | = | nondimensional side-load time |
| $\Phi_{\mathrm{sl}}$ | = | nondimensional side-load force |
| $\chi$ | = | secondary-to-primary mass flow rate ratio, $\dot{m}_f/\dot{m}_m$ |

*Subscripts*

| | | |
|---|---|---|
| $a$ | = | ambient |
| $b$ | = | base, value at the end of the base |
| $c$ | = | combustion chamber |
| $e$ | = | extension, nozzle exit |
| $f$ | = | film flow, film injection cross section |
| fb | = | film breaking |
| $i$ | = | inflection region |
| $m$ | = | main flow |
| $o$ | = | overall nozzle |
| $r$ | = | recovery value |
| $s$ | = | separation point |
| $t$ | = | throat |
| $w$ | = | wall |

Presented as Paper 5207 at the 42nd AIAA/ASME/SAE/ASEE Joint Propulsion Conference and Exhibit, Sacramento, CA, 9–12 July 2006; received 19 June 2008; revision received 18 December 2008; accepted for publication 24 June 2009. 

*Research Fellow, Department of Mechanics and Aeronautics, via Eudossiana 18. Member AIAA.

†Associate Professor, Department of Mechanics and Aeronautics, via Eudossiana 18. Senior Member AIAA.

‡Professor, Department of Mechanics and Aeronautics, via Eudossiana 18. Senior Member AIAA.

## I. Introduction

THE key demand on future space transportation systems is the concurrent reduction of Earth-to-orbit launch costs and increase of launcher reliability and operational efficiency. A common way of slightly improving performance of gas-generator open-cycle engines is the injection of the turbine exhaust gas (TEG) into the main nozzle. The role of TEG injection is twofold: in addition to the performance increase, it provides a low-temperature gas that is able to create an insulating film that reduces the convective heat transfer rate from the hot-gas stream to the exposed nozzle surface. To get advantages from both sides, the TEG injection system must be properly designed. In particular, several studies on film cooling [1–3] have shown that the highest efficiency is obtained when the coolant fluid is injected parallel to the primary stream to minimize the mixing, which tends to break down the insulating film, thus reducing coolant efficiency. In addition, it has been shown that film cooling is much more efficient in supersonic than in subsonic flows, because the former presents a thinner boundary layer, smaller turbulent length scales, and thus a lower mixing rate than the latter [3].

The basic studies on TEG injection have addressed cooling properties and nozzle performance during design operations in conventional nozzles. However, following the recent development in advanced nozzle studies [4,5], a further aspect to investigate is the role of film injection in nozzles designed to operate with steady separated flow during the first part of the launch. To this goal, a first study has been carried out by the authors [6] regarding a parametric analysis of the film cooling of a subscale dual-bell nozzle (Fig. 1). The divergent section of this advanced nozzle features two bells with different exit areas to allow safe operation with separated flow at low altitude [5,7,8].

This work aims to study the efficiency of the film cooling in a hot full-scale dual-bell nozzle, with the injection made upstream of the inflection point between the two bells. This analysis is carried out in the simpler case of high-altitude operation, which shows attached flow in the whole nozzle, considering the effect of secondary mass flow rate and of the height of the film-cooling slot. The results suggest

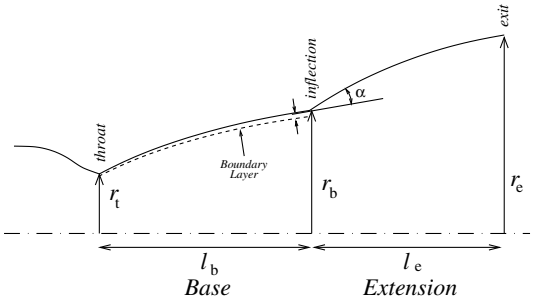


**Fig. 1 Schematic of a dual-bell nozzle.**

that film cooling can be very efficient, due to the centered expansion at the inflection. But secondary gas injection might also have a negative effect on the overexpanded operation of the nozzle, for which it could enhance the strength of side loads. This aspect is studied starting from a qualitative analysis of the influence of the film cooling on the expected evolution of the separation point in the inflection region, which is characterized by a negative value of the wall pressure gradient as in conventional nozzles and can therefore favor the onset of side loads [9]. The numerical simulations are carried out by a multicomponent Reynolds-averaged Navier–Stokes equations solver, for which the capability of describing the turbulent compressible mixing layer has been proved by comparison with experimental data available in literature [6,9].

## III. Dual-Bell Nozzles

The existence of a discontinuity of the nozzle contour defines the peculiar dual-bell shape dividing the divergent section in an upstream part, the base, and a downstream part, the extension (Fig. 1); in particular, from one side, this shape permits achieving the larger expansion ratio required for an efficient nozzle, and from the other side, it forces the separation-line position in the proximity of the discontinuity in the highly overexpanded condition that takes place at sea level. Therefore, the dual-bell nozzle features two different operating modes, relevant to two different adaptation altitudes. At low altitude, in the first operating mode (OM1), the flow is attached in the base and separated downstream of the inflection point. In this case, the separation point is placed in a precise location, the inflection point, and thus a symmetrical separation takes place that guarantees a low level of side loads compared with the case of bell nozzles, for which separation is not forced by geometry. At high altitude (OM2), the nozzle operates with attached flow in the whole divergent section. Therefore, the limitation of nozzle expansion ratio due to sea-level-operation side loads is circumvented and, consequently, a higher vacuum specific impulse than bell nozzles (which display a single adaptation altitude) is obtained. Nevertheless, side loads also remain a concern for the dual-bell nozzle design because of their possible occurrence both during OM1 and during transition to OM2, as confirmed by numerical and experimental studies [10–13]. In fact, in the ideal case, the discontinuity between the two bells causes a step in the wall pressure behavior, then during the first operating mode, the separation point is anchored at the discontinuity, avoiding the onset of side loads. In the real case, due to viscosity, the ideal step becomes a region of finite length (Fig. 2) in which the pressure gradient is negative, as in conventional nozzles [14]. In this region, spanning from the inflection point to the point at which pressure is minimum in OM2 and defined as inflection region [14], the separation point may find stable but not symmetric equilibrium positions because of the inevitable internal flow or external pressure environment asymmetries. Thus, in addition to the evaluation of possible side loads caused by OM1 to OM2 transition, the intensity and duration of side loads generated in the inflection region during OM1 must be carefully studied.

## III. Film-Cooling Test Cases

All test cases that will be discussed in the following concern a reference hot full-scale dual-bell nozzle with the base designed as a truncated ideal contour and with the properties reported in Table 1. The area ratios of the base and the extension have been chosen according to [15].

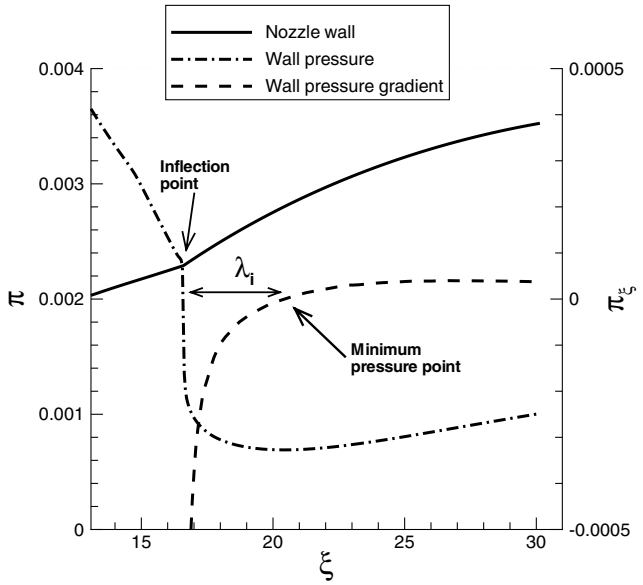


**Fig. 2 Wall pressure behavior in the extension of a linearly increasing wall pressure dual-bell nozzle and definition of inflection region $\lambda_i$.**

The extension features a linearly increasing wall pressure; therefore, the wall pressure behavior downstream of the inflection shows a negative wall pressure gradient (the inflection region), a minimum wall pressure value, and a region of positive gradient, as displayed in Fig. 2. The latter zone serves to guarantee a fast transition between the two operating modes [14].

In the film-cooled dual-bell nozzle, the injection is made through an axisymmetric slot located in the divergent section of the base at $\xi_f = 10$, where area ratio is $\epsilon_f = 28$, and the near-wall main Mach number is $M_m = 3.79$. Two different slots are selected, for which the nondimensional heights are $\sigma = 0.11$ and 0.08, respectively. The injection is made at a supersonic velocity and the film flow is characterized by a large inviscid core. The mixing with the main flow occurs first through a mixing layer, which eventually merges with the wall boundary layer. Before merging occurs, the adiabatic wall temperature remains equal to the recovery value of the cold flow. Downstream, the wall begins to be affected by mixing of hot and cold streams, the so-called film breaking occurs, and adiabatic wall temperature starts increasing. Thus, an important role in film-cooling efficiency is played by the mixing-layer spreading rate, mainly depending on film and main flow Mach number and on secondary-to-primary mass flow ratio $\chi$ [16]. For each slot height, the mass flow rate is changed by varying the film Mach number, temperature, and total pressure, while keeping the film total temperature and static pressure constant. The latter value is selected to have the film static pressure matched with the main flow static pressure.

**Table 1 Geometric and combustion chamber data of the reference full-scale dual-bell nozzle**

| Parameters | Values |
|---|---|
| Throat radius $r_t$, m | 0.1 |
| Chamber temperature $T_c$, K | 3500 |
| Chamber pressure $p_c$, MPa | 12 |
| Nondimensional base length $\lambda_b$ | 16.6 |
| Nondimensional extension length $\lambda_e$ | 14.3 |
| Nondimensional divergent section length $\lambda_o$ | 30.9 |
| Base area ratio $\epsilon_b$ | 48 |
| Overall area ratio $\epsilon_o$ | 115 |
| Oxidizer-to-fuel mass ratio $O/F$ | 6 |
| Inflection angle $\alpha$, deg | 13.68 |
| Chamber Reynolds number $Re_c = \rho_c a_c r_t/\mu_c$ | $1.044 \times 10^7$ |
| Nondimensional extension-design wall pressure gradient $\pi_{\xi,e}$ | $3 \times 10^{-5}$ |

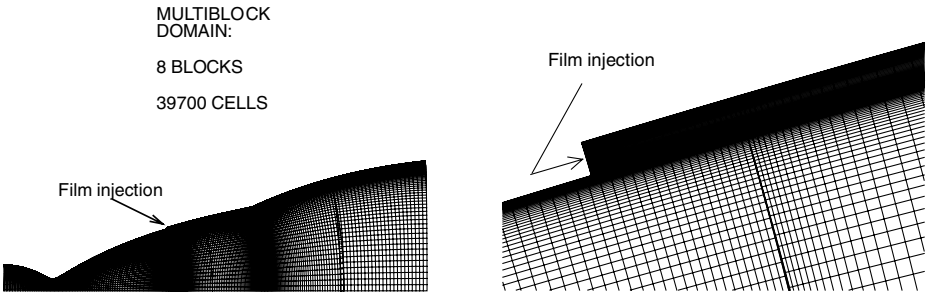


**a) Computational domain** **b) Mesh enlargement at film injection**

**Fig. 3 Computational grid.**

## IV. Numerical Approach, Computational Domain, and Boundary Conditions

The analysis of the dual-bell nozzle flowfield is performed by a 2-D axisymmetric time-accurate multispecies-reacting Reynolds-averaged Navier–Stokes solver, based on the approach described in [9,17,18]. The main features of this method are to discretize the convective terms according to the lambda scheme developed by Moretti [19]. The discontinuities are solved via a finite volume Godunov method (hybrid formulation [9,20]). The viscosity and conductivity of the single species are described by Sutherland's law and the mixture properties are derived from Wilke's rule. Turbulence is computed by a modified version [21] of the Spalart–Allmaras [22] one-equation model, which takes into account the compressibility effects. This is an important characteristic when studying the film cooling in a supersonic stream, because the spreading of the mixing layer is affected by compressibility effects and its exact prediction is crucial to determine the effectiveness of the film cooling [23,24]. The ability of the present model to predict the spreading rate has been demonstrated in [6]. On the other hand, the compressibility correction limits the production term in the turbulence equation, yielding a significant difference in the computation of the skin friction (up to 15%) and a markedly more acceptable difference in the prediction of adiabatic wall temperature (lower than 1%), which is the most interesting parameter in the present study. The error in the prediction of skin friction is considered to be of minor importance in the present study, in which no separated-flow simulations are carried out, with respect to the necessity of correctly describing the mixing-layer spreading rate.

The computational domain is defined by the nozzle geometry. The nozzle is characterized by subsonic inflow boundary conditions describing the combustion chamber (total temperature and total pressure are enforced together with the flow direction and chemical composition), supersonic outflow, symmetry axis, and adiabatic wall. The inlet flow is a mixture of $H_2O$ and $H_2$, deriving from the complete depletion of the oxygen and from the selected fuel-rich mixture ($O/F = 6$). Finally, at the supersonic film injection inlet static pressure, static temperature, Mach number, chemical composition, and flow direction are enforced. For the sake of simplicity, the chemical composition of the film is assumed to be equal to that of the main flow.

A multiblock grid (Fig. 3a) is used to suitably distribute cell density. In particular, in the vicinity of the injection point, the cells are clustered in the wall normal direction to correctly describe the wall boundary layers and the mixing layer (Fig. 3b). Moreover, clustering in the streamwise direction has been applied to increase the accuracy in the first part of the mixing layer, in which large streamwise gradients take place. To simulate the slot for the secondary gas injection, the wall profile is translated outward from the injection point to the nozzle end.

## V. Discussion of the Results

A parametric analysis of dual-bell nozzle film cooling has been carried out by considering different combinations of film Mach number and slot height. In particular, as the total temperature is the same for all the tests, each value of Mach number is associated with a value of film static temperature. Moreover, each test is also associated with a value of mass ratio $\chi$, for which the typical flight

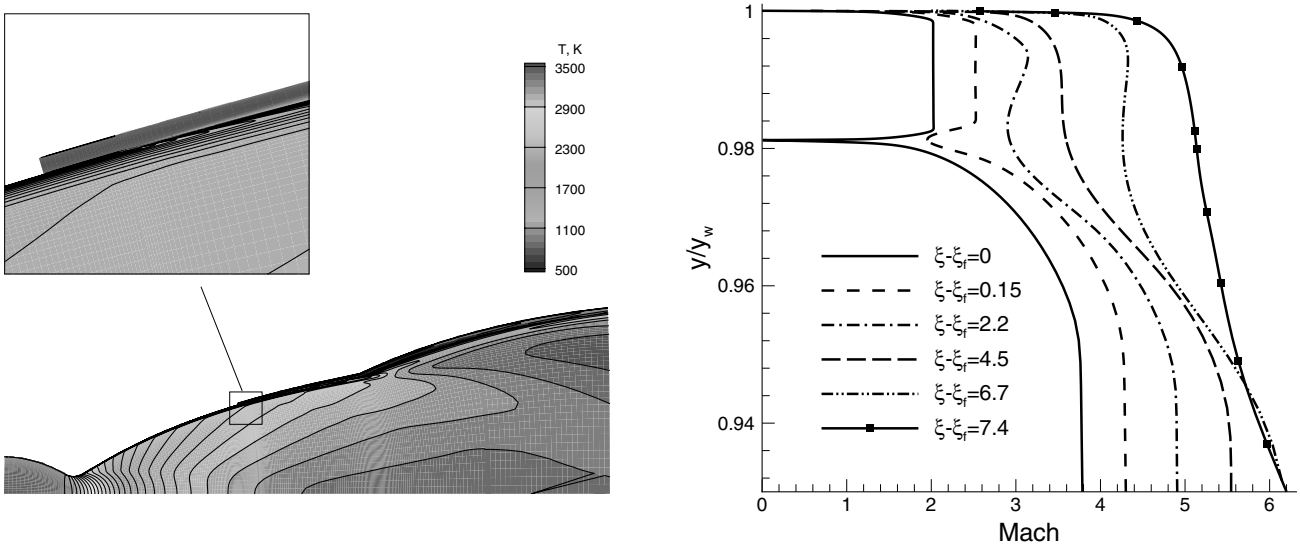


**a) Temperature flowfield** **b) Boundary-layer and mixing-layer profiles at various distances from the injection**

**Fig. 4 Temperature flowfield and boundary- and mixing-layer profiles for the film cooling with $T_f = 450$ K, $M_f = 2$, and $\sigma = 0.11$.**

**Table 2 Secondary flow conditions**

| $\sigma = 0.11$ | | | $\sigma = 0.08$ | | |
|---|---|---|---|---|---|
| $T_f$, K | $M_f$ | $\chi$ | $T_f$, K | $M_f$ | $\chi$ |
| 640 | 1.01 | 0.025 | 640 | 1.01 | 0.018 |
| 604 | 1.20 | 0.030 | 604 | 1.20 | 0.022 |
| 565 | 1.40 | 0.037 | 565 | 1.40 | 0.027 |
| 525 | 1.60 | 0.044 | 525 | 1.60 | 0.032 |
| 487 | 1.80 | 0.051 | 487 | 1.80 | 0.037 |
| 450 | 2.00 | 0.059 | 450 | 2.00 | 0.043 |

values (for instance, $\chi = 0.03$ for the Vulcain 2[§] engine) are included in the range examined. As an example of the results computed with the present approach, a temperature flowfield of a film-cooled dual-bell nozzle is shown in Fig. 4a for the case with chamber and nozzle data reported in Table 1 and film cooling featuring the following properties: $T_f = 450$ K, $M_f = 2$, and $\sigma = 0.11$. The expansion waves generated by the inflection point are clearly visible in the figure. The mixing layer between the secondary and the main streams can be seen in the enlargement. Figure 4b shows the boundary- and mixing-layer profiles at different axial stations, starting from the injection point $\xi_f$. The radial distance from the axis of symmetry is normalized with the nozzle contour radius, and each Mach number profile is translated by a quantity of 0.5 for clarity reasons. The two layers gradually evolve up to merge in a single layer.

The list of input data for the different test cases carried out in the parametric analysis is reported in Table 2. The different flow velocities and mass flow rates yield different wall temperature behaviors along the film-cooled wall (Fig. 5). In particular, immediately downstream of the injection point, the adiabatic wall temperature is the recovery temperature of the coolant. This temperature level is maintained nearly constant until the mixing layer merges with the wall boundary layer. From this point onward the wall is influenced by the hot-gas total temperature value, and the wall temperature rises. Increasing the secondary-to-primary mass flow rate ratio has the effect of moving the merging point of the layers downstream and of reducing the maximum wall temperatures, which are reached at the nozzle exit. In fact, they decrease from 1836 to 1061 K for $\sigma = 0.11$ and from 2053 to 1360 K for $\sigma = 0.08$, for increasing values of $\chi$.

It is interesting to note that just downstream of the inflection point ($\xi = 16.6$) the adiabatic wall temperature shows a sudden decrease and then starts increasing again with a lower rate. The sudden decrease and reduced mixing are caused by the expansion at the inflection. In fact, the local Mach number increases and, as a consequence, the wall recovery temperature reduces, as can be seen in Fig. 6 for a case without film cooling. In addition, the increase of the local convective Mach number reduces the mixing spreading rate [3]. This property helps the film to cool the wall for a longer distance.

### A. Film-Cooling Efficiency

Comparison of the results is made easier by introducing the film-cooling efficiency [1]. For compressible flows, it is defined as

$$\eta = \frac{T_w - T_r}{T_{w,f} - T_r} \tag{1}$$

where $T_w$ is the adiabatic wall temperature, $T_{w,f}$ is its value at the film injection, and $T_r$ is the recovery temperature of the wall without film cooling. At the injection, the efficiency is equal to 1, indicating that the wall is isolated from the hot stream. After the merging of the mixing layer with the wall boundary layer, the efficiency starts decreasing. The parameter $\eta$ is useful to correlate data when the numerical results are reported in a log–log scale as a function of a suitable correlation parameter. According to [2], it can be seen that when dealing with the mixing of flows with different thermophysical properties, a good correlation parameter is the following:

$$\frac{\xi - \xi_f}{\beta\sigma}\frac{c_{p,m}}{c_{p,f}}$$

which includes the axial distance from the injection point $\xi - \xi_f$, the slot height $\sigma$, the blowing ratio $\beta = (\rho u)_f/(\rho u)_m$, and the ratio of the constant-pressure specific heat $c_{p,m}/c_{p,f}$.

In Fig. 7a the film-cooling efficiencies are reported as a function of the correlation parameter. It can be seen that the data do not collapse, due to the scattering effect of the expansion fan. But if only the efficiencies computed upstream of the inflection point are displayed (as shown by the enlargement in Fig. 7b), data cluster around a single curve. An exponential law can be then interpolated for the decaying part of $\eta$:

$$\eta = 4.768\left(\frac{\xi - \xi_f}{\sigma\beta}\frac{c_{p,m}}{c_{p,f}}\right)^{-0.38} \tag{2}$$

This correlation could be useful to predict, in a first approximation, the efficiencies of those cases for which the data are in the range used in this study. The collapsed results permit individuating the values of the correlation parameter at the film breaking point. This point is defined as the abscissa downstream of the injection point at which the efficiency becomes lower than 0.95. The behavior of $\xi_{fb}$ as a function

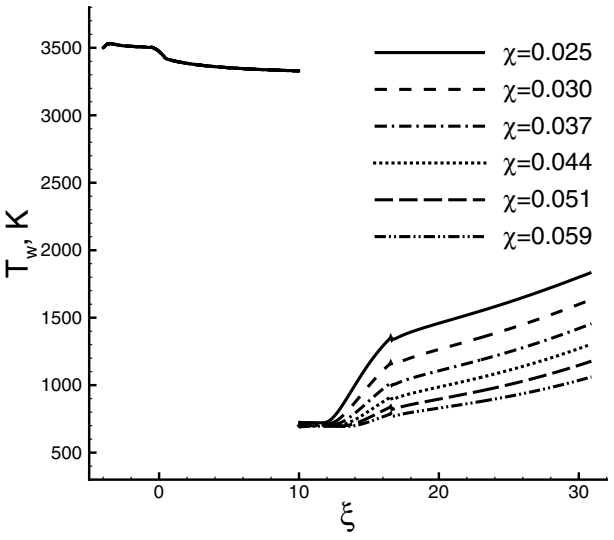


**a) σ = 0.11**

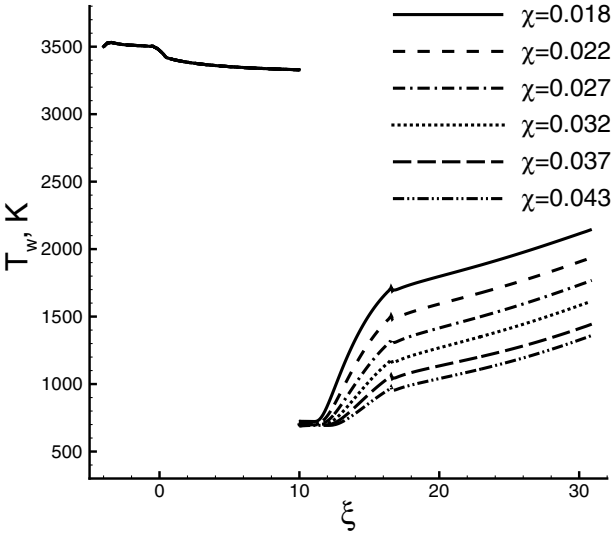


**b) σ = 0.08**

**Fig. 5 Wall temperature profiles for varying $\sigma$ and $\chi$.**

[§]Data available online at http://cs.astrium.eads.net/sp/LauncherPropulsion/Vulcain-2-Rocket-Engine.html [retrieved 9 August 2009].

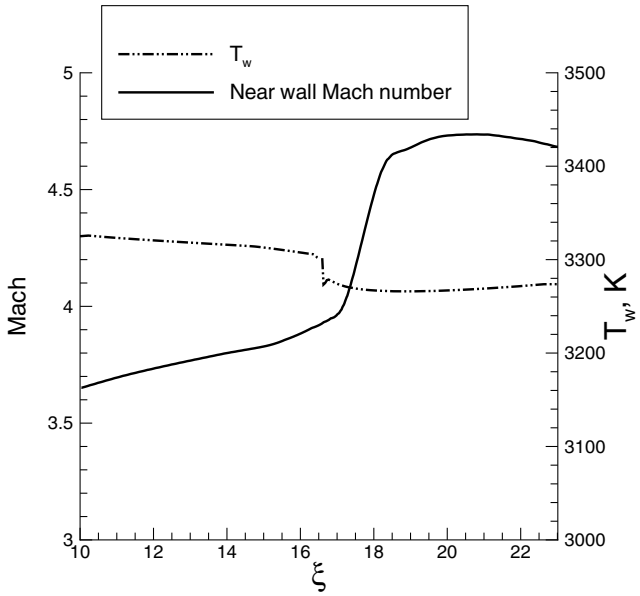


**Fig. 6 Near-wall Mach number and adiabatic wall temperature (without film) profiles.**

of $\chi$ is a direct consequence of the results shown in Fig. 7b. In particular, the parametric analysis shows that increasing $\chi$ or the slot height shifts the film breaking point downstream, as can be clearly seen in Fig. 8. This can be attributed to the higher momentum or to the larger dimension of the inviscid core downstream of the slot: the hot gas must travel a further distance to penetrate up to the wall surface.

### B. Film-Cooling Effect on the Inflection Region

The injection of a secondary gas in the main stream has the major effect of modifying the flowfield properties near the wall. In particular, the wall pressure behavior is noticeably different with respect to the case with no film cooling. The wall pressure and its gradient, shown for the different cases in Fig. 9, indicate that the inflection region is altered by the presence of the film cooling and that the modification is greater when $\chi$ increases.

The test case with the smallest slot height yields a lower alteration, as shown by the pressure gradient behaviors for $\xi$ between 16.8 and 18. Moreover, in both cases, the minimum value of the wall pressure at the end of the expansion increases for increasing $\chi$ and the inflection region enlarges (Figs. 9 and 10). Its nondimensional length

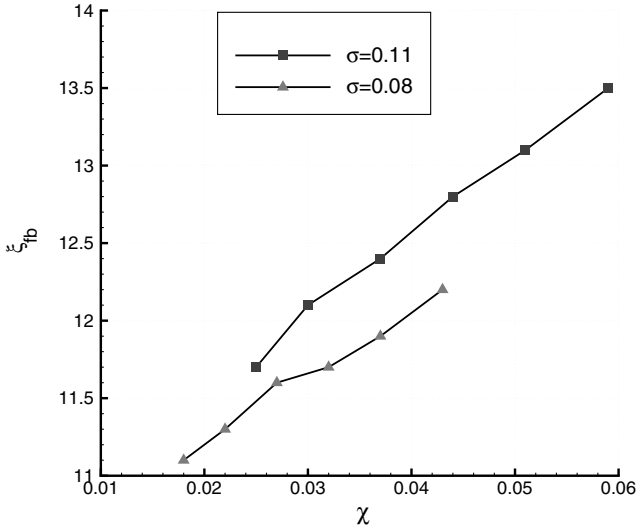


**Fig. 8 Film breaking point $\xi_{fb}$ versus secondary-to-primary flow mass ratio.**

$\lambda_i$ is only slightly affected by the value of slot height. In particular, $\lambda_i = 3.78$ in the case of no film injection, whereas when $\chi = 0.018$, which is the lowest value considered, $\lambda_i$ raises to 4.74. Then further increasing $\chi$, the inflection region enlarges, reaching a value of 5.52 times the throat radius for $\chi = 0.059$. The influence of the film cooling on the inflection region can be explained following the arguments reported in a previous work of the authors [10], in which it was argued that the nondimensional inflection-region length $\lambda_i$ is a function (among other parameters) of the wall Mach number and the specific heat ratio $\gamma$ at the inflection point. The injection of a secondary gas changes these parameters, and as a consequence, the wall pressure behavior in the extension is affected.

In Fig. 10 the wall temperature at the nozzle lip is also reported as a function of the secondary-to-primary mass flow ratio. It obviously decreases as $\chi$ increases, and in the most favorable case, $T_{w,e} = 1061$ K. This figure also shows that there is only a minor effect of $\sigma$.

## VI. Side-Load Analysis

The properties of the inflection region have been discussed, with particular emphasis devoted to the effect of film cooling on its

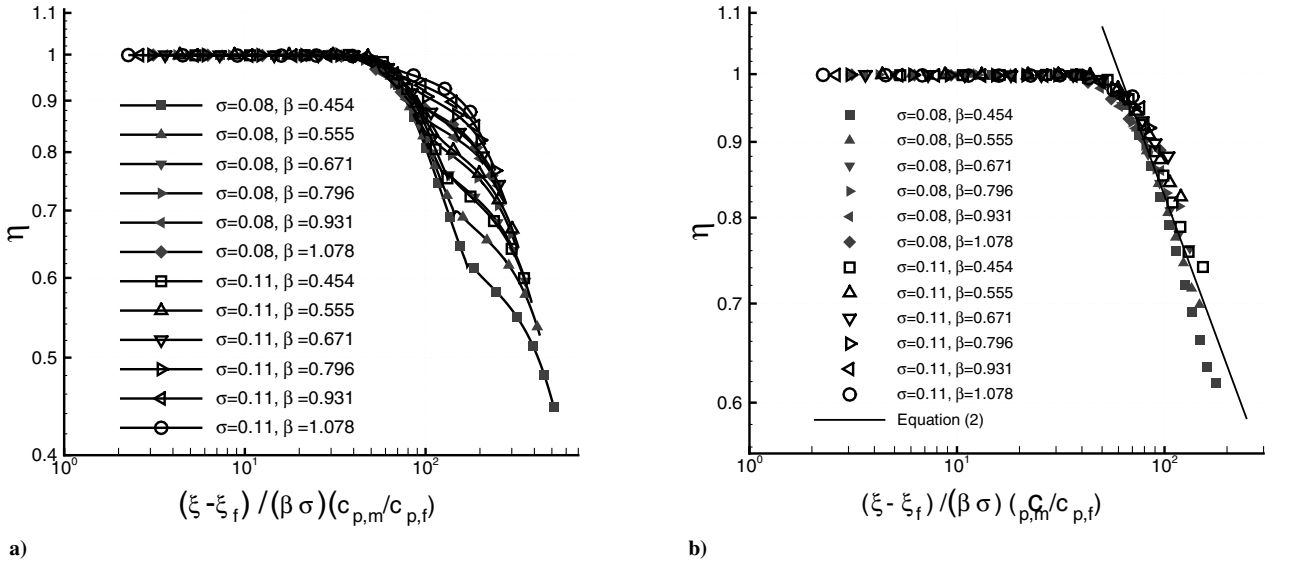


**Fig. 7 Plots of a) film-cooling efficiency as a function of the correlation parameter and b) enlargement of the data computed upstream of the inflection point and comparison with correlation (2).**

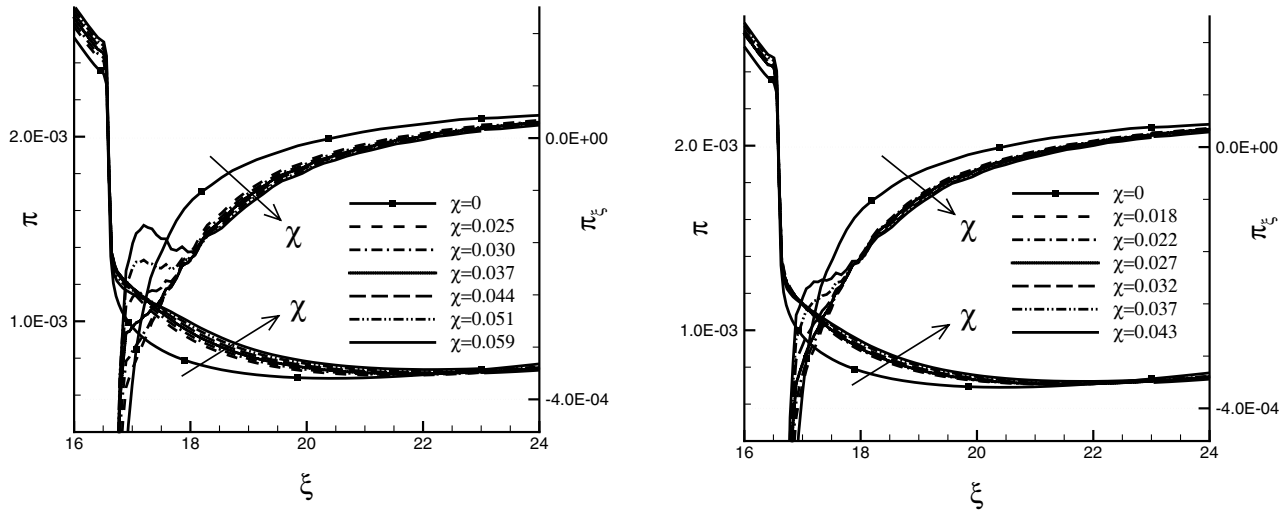


**Fig. 9 Wall pressure and its gradient in the inflection region for varying χ.**

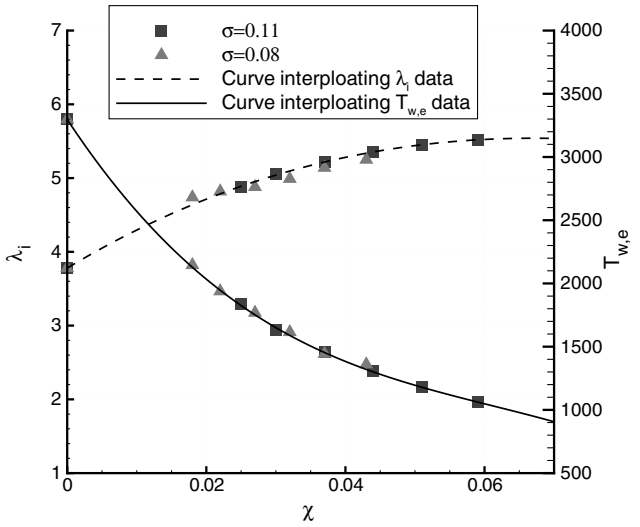


**Fig. 10 Inflection-region extension and exit wall temperature versus secondary-to-primary mass flow ratio.**

dimension. In addition to this aspect, it is worthwhile to evaluate how film cooling can affect the side loads that are expected to take place because of the existence of the inflection region. Although side loads are due to the three-dimensional and unsteady character of the wall pressure field [25–28], a preliminary evaluation of their intensity can be made following the approach already proposed in [10]. This approach provides an evaluation of side loads that take place during OM1, when the separation point lies in the inflection region. To better clarify why attention is paid to the onset of side loads during OM1, it is useful to make a gross estimation of the time spent with the separation point in the inflection region during a typical launcher ascent. This can be made following the approach of [8], which leads to the conclusion that this time interval is of the order of 10 s [10]. Within the present approach, according to Schmucker [29], the side load can be modeled as in conventional overexpanded nozzles by a bias of the separation line from its averaged symmetric position. The resulting nondimensional side load $\Phi_{sl}$, due to the unsymmetrical separated area, is evaluated as

$$\Phi_{sl} = K_{sl}\left(\frac{r_s}{r_t}\right)\frac{\mathcal{F}_1(M_s,\gamma)}{|\pi_{\xi,s}|} \tag{3}$$

where $\pi_{\xi,s}$ is the nondimensional attached-flow wall pressure gradient at the separation-point abscissa; $r_s$ is the average nozzle radius at the separation point; $K_{sl}$ is a nondimensional constant for which the value, in the case of conventional nozzles, can be obtained by those of constants introduced in [29]; and $\mathcal{F}_1$ is a nondimensional expression depending on the flow Mach number and $\gamma$ outside of the boundary layer at the separation point. As the value of the length of the unsymmetrical separated area is proportional to $\pi_\xi^{-1}$, the wall pressure gradient is the most important factor that influences the side load. It is worth remembering that Eq. (3) is only valid when $\pi_\xi < 0$ and provides an empirical law for the prediction of side loads when the separation point is placed at a specific wall position (featuring a value of $M_s$, $\pi_s$, and $\pi_{\xi,s}$) because of the specific ambient pressure and chamber pressure values. The application of Eq. (3) is straightforward for conventional nozzles, whereas it must be more carefully considered in the case of dual-bell nozzles, in which the values outside the boundary layer of the attached-flow viscous solution should be considered as input for Eq. (3). In fact, the side-load strength is determined by the actual finite value of $|\pi_\xi|$ in the finite inflection region, in which $\pi_\xi$ is negative. Note that because of the small value of $|\pi_\xi|$, a high level of side loads is expected during OM1, when the separation point lies in the inflection region. To make a comparative evaluation of the importance of side loads in terms of time of flight trajectory during which a large level of lateral forces is expected, a critical time interval is introduced. This critical time interval is defined as the part of the launch phase during which the separation wall pressure is in the range such that $\Phi_{sl}$ varies between a threshold value (say, 0.02) and the maximum value. This threshold value is selected arbitrarily only for the sake of comparison among the different cases that will be examined. These separation wall pressure ranges can be translated into the corresponding ambient pressure range by the separation criterion of Schmucker [30]:

$$\Delta\pi_a = \pi_{a,1} - \pi_{a,2} \tag{4}$$

where $\pi_{a,1}$ equals the value of $\pi_a$ when $\Phi_{sl} = 0.02$, and $\pi_{a,2}$ equals the value of $\pi_a$ when $\Phi_{sl} = \Phi_{sl,max}$. From this relationship and the hypotheses of isothermal atmosphere and constant launch vehicle velocity $V$ in the present range of ambient pressure [10], the critical time interval can be computed as

$$\tau_{sl} = \frac{t_{sl}}{(R_a T_a)/(gV)} = -\ell_n\left(1 - \frac{\Delta\pi_a}{\pi_{a,1}}\right) \tag{5}$$

The two parameters $\Phi_{sl}$ and $\tau_{sl}$ have been evaluated to analyze the properties of side loads in the case of film-cooled dual-bell nozzles for varying slot height and mass flow rate (Fig. 11). The first two plots, Figs. 11a and 11b, report the nondimensional side-load intensity $\Phi_{sl}$ versus the nondimensional ambient pressure $\pi_a$ (that is,

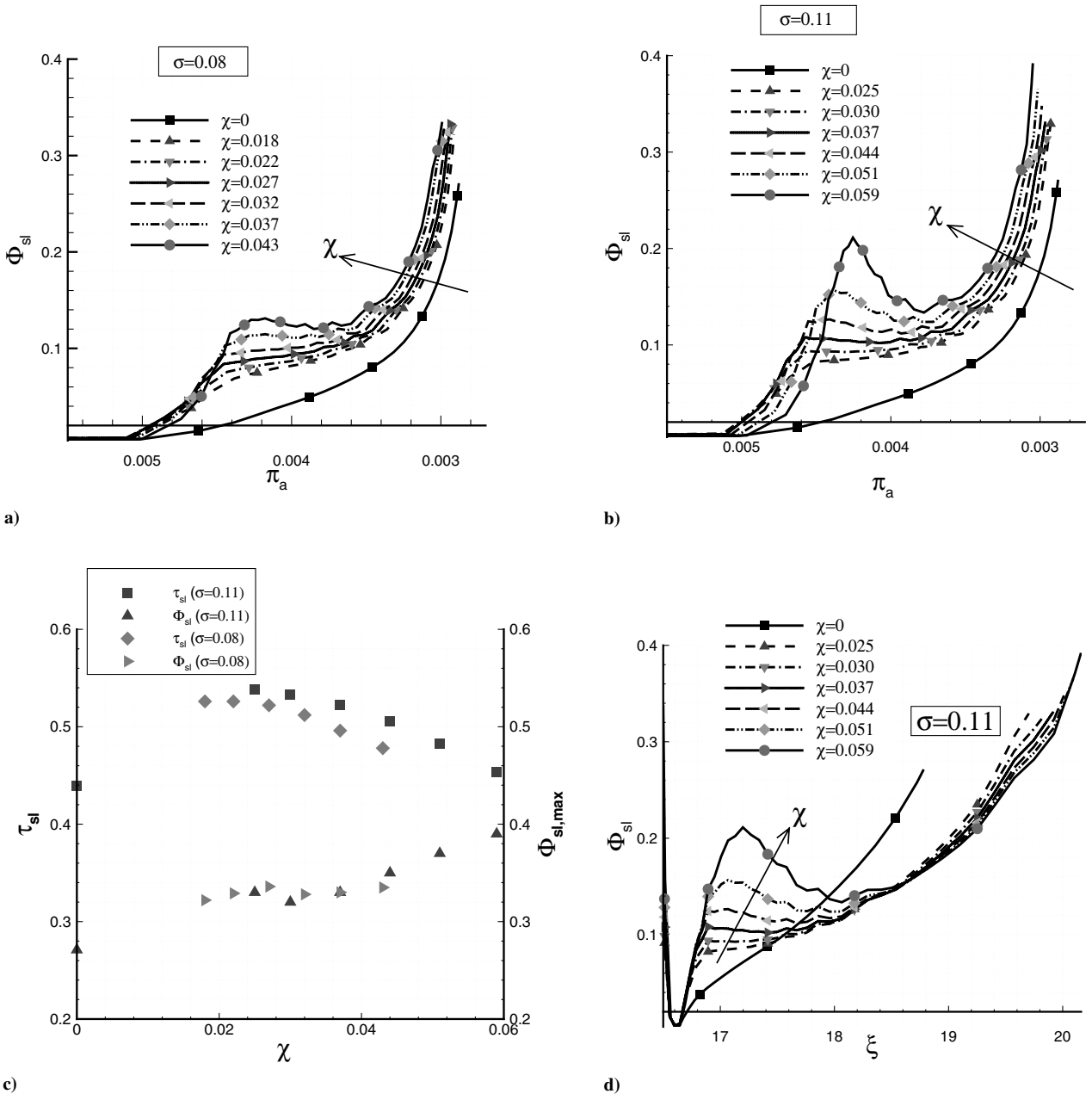


**Fig. 11 Side loads due to interaction between film cooling and flow separation.**

altitude) for the two values of slot height and with the secondary-to-primary mass flow ratio $\chi$ as a parameter, including the case with no film cooling ($\chi = 0$) for the sake of comparison. The axis of abscissas is located at $\Phi_{sl} = 0.02$, which is the threshold value. For a certain range of ambient pressures, the side-load level is nearly zero; the separation point is forced to be anchored at the inflection point by the very high negative pressure gradient of the expansion fan. When the ambient pressure decreases, the separation point moves downstream and enters the region in which the wall pressure gradient tends to zero. As a consequence, the lateral force starts increasing, reaching a maximum near the minimum pressure point. In the case with no film cooling, the curve shows a monotonic increase, and the higher values of the side force are reached at the end of the OM1 (i.e., at the lowest value of $\pi_a$ considered). The injection of a secondary gas changes this behavior: the side-load intensity shows a first sudden increase for $0.0050 \gtrsim \pi_a \gtrsim 0.0045$, then a plateau or a reduction in the range of $0.0045 \gtrsim \pi_a \gtrsim 0.0035$, and for $\pi_a \sim 0.0030$, it reaches a maximum at the limit of the interval considered to compute $\Phi_{sl}$. In the case with larger nondimensional slot height (Fig. 11b), the plateau tends to become a relative maximum as $\chi$ increases.

Figure 11c reports the values of maximum nondimensional side load $\Phi_{sl,max}$ and of the time duration of side forces $\tau_{sl}$. As far as $\Phi_{sl,max}$ is concerned, it can be seen that with the film cooling, the maximum value slightly increases with respect to the case with no injection. For $\sigma = 0.11$, as $\chi$ increases, $\Phi_{sl}$ increases, whereas for $\sigma = 0.08$, the maximum values practically remain unchanged, even if they are all higher than the maximum value with no film cooling. The increase ranges from 18 and 19% to 44 and 24%, for $\sigma = 0.11$ and 0.08, respectively. Looking at the $\tau_{sl}$ parameter, the data show that the critical time interval slightly increases with the film cooling with respect to the case with no film cooling (from 2.2 to 23% for $\sigma = 0.11$ and from 9 to 20% for $\sigma = 0.08$). It is interesting to note that as $\chi$ increases, $\tau_{sl}$ decreases, even if the inflection-region length increases. Figure 11d shows the values of $\Phi_{sl}$ as a function of the separation-point position $\xi_s$ in the inflection region. As $\chi$ increases, side loads occur for a larger part of the extension, just due to the enlargement of $\lambda_i$. The observed time reduction is due to the fact that increasing the secondary-to-primary mass flow ratio increases the minimum wall pressure value (Fig. 9). This higher minimum wall pressure value corresponds to a higher ambient pressure value (and to a lower

altitude) during the ascent; thus, the value of $\pi_{a,2}$ increases and the ambient pressure interval $\Delta\pi_a$ shrinks.

The final comment to the present results is that the duration of side loads is of the same order of magnitude as that obtained without film cooling, but it must be considered that during this time the average side-load level is increased by film-cooling mass flow. This result should not be underestimated because the side-load duration may be rather long (on the order of 10 s) if typical launcher trajectory values are considered [10].

## VII. Conclusions

The analysis carried out in this study shows that the supersonic injection of a secondary stream can efficiently cool the wall of a dual-bell nozzle. Moreover, when the injection is made in the base, the expansion generated by the inflection point lowers the wall recovery temperature, reduces the mixing, and allows the film to protect the wall for a longer distance. The maximum wall temperature of the cooled wall, reached at the nozzle lip, decreases significantly when the secondary-to-primary mass flow rate ratio is increased. It has been found to be a good correlation parameter that is obtained by a combination of the axial distance from the injection point, the slot height, the blowing ratio, and the ratio of the constant-pressure specific heats. This parameter has permitted clustering the film-cooling efficiencies around a single curve and finding an exponential law that can be useful to predict, in a first approximation, the efficiencies for those cases for which the conditions are in the range used in this work.

The numerical results also show that the presence of a secondary gas modifies the thermophysical properties of the flowfield in the proximity of the nozzle contour and changes the wall pressure behavior in the inflection region, for which the properties determine the level and duration of side loads, which could last several seconds during the launcher ascent. In particular, the presence of the film cooling causes the enlargement of the inflection region, for which the length increases for increasing cooling mass flow rate. However, the duration and intensity of significant side loads during the final phase of the OM1 are barely affected by film cooling. The duration, longer that in the case of uncooled nozzle, slightly decreases for increasing coolant mass flow and decreasing slot height. Side load intensity shows a tendency of a slight increase for increasing cooling mass flow rate, whereas it is not significantly affected by the slot height. As a final remark, it can be said that even if these lateral forces are expected to be lower than those possibly occurring during the transition between the two operating modes, they are characterized by a greater time period (long-lasting side loads), with possible excitation of nozzle structural modes of vibration. On the other hand, it has to be considered that film cooling has recently been proposed as a device to favor the rapid transition from OM1 to OM2 in dual-bell nozzles [31]. However, this use of film cooling requires the study of the interaction of the film injection with the dynamics of the separation point and has to be considered for future developments.

## References


[1] O'Connor, J. P., and Haji-Sheikh, A., "Numerical Study of Film Cooling in Supersonic Flow," *AIAA Journal*, Vol. 30, No. 10, Oct. 1992, pp. 2426–2433. doi:10.2514/3.11243

[2] Juhany, K. A., Hunt, M. L., and Sivo, J. M., "Influence of Injectant Mach Number and Temperature on Supersonic Film Cooling," *Journal of Thermophysics and Heat Transfer*, Vol. 8, No. 1, Jan.–March 1994, pp. 59–67 . doi:10.2514/3.501

[3] Aupoix, B., Mignosi, A., Viala, S., Bouvier, F., and Gaillard, R., "Experimental and Numerical Study of Supersonic Film Cooling," *AIAA Journal*, Vol. 36, No. 6, June 1998, pp. 915–923. doi:10.2514/2.495

[4] Muss, J. A., Nguyen, T. V., Reske, E. J., and McDaniels, D. M., "Evaluation of Altitude Compensating Nozzle Concepts for RLV," 33rd AIAA/ASME/SAE/ASEE Joint Propulsion Conference and Exhibit, AIAA Paper 97-3222, July 1997.

[5] Hagemann, G., Immich, H., Nguyen, T. V., and Dumnov, G. E., "Advanced Rocket Nozzles," *Journal of Propulsion and Power*, Vol. 14, No. 5, Sept.–Oct. 1998, pp. 620–634. doi:10.2514/2.5354

[6] Nasuti, F., Martelli, E., Onofri, M., and Pietropaoli, E., "Film Cooling in Dual Bell Nozzle," *Proceedings of the 5th European Symposium on Aerothermodynamics for Space Vehicles*, ESA SP-563, European Space Research and Technology Centre, Noordwijk, The Netherlands, 2005.

[7] Horn, M., and Fisher, S., "Dual-Bell Altitude Compensating Nozzle," NASA CR-194719, 1994.

[8] Hagemann, G., Frey, M., and Manski, D., "A Critical Assessment of Dual-Bell Nozzles," 33rd AIAA/ASME/SAE/ASEE Joint Propulsion Conference and Exhibit, AIAA Paper 97-3299, July 1997.

[9] Martelli, E., Nasuti, F., and Onofri, M., "Numerical Parametric Analysis of Dual-Bell Nozzle Flows," *AIAA Journal*, Vol. 45, No. 3, March 2007, pp. 640–650. doi:10.2514/1.26690

[10] Martelli, E., "Studio Della Fluidodinamica Interna di Ugelli Propulsivi di Tipo Dual Bell," Ph.D. Dissertation, Univ. of Rome "La Sapienza," Rome, Jan. 2006.

[11] Perego, D., and Schwane, R., "Simulation of Unsteady Three Dimensional Separation Behaviour in Truncated Ideal Contour Nozzle," 40th AIAA/ASME/SAE/ASEE Joint Propulsion Conference, AIAA Paper 2004-4015, July 2004.

[12] Hieu Le, T., Girard, S., and Alziary de Roquefort, T., "Direct Measurement of Side Loads with Transonic Bueting," *Proceedings of the 5th European Symposium on Aerothermodynamics for Space Vehicles*, ESA SP-563, European Space Research and Technology Centre, Noordwijk, The Netherlands, 2005.

[13] Nürnberger-Gnin, C., and Stark, R., "Experimental Study on Dual-Bell Nozzle," *Proceedings of the 2nd European Conference for Aerospace Sciences* [CD-ROM], von Karman Inst. for Fluid Dynamics, Rhode-St.-Genèse, Belgium, 1–6 July 2007.

[14] Nasuti, F., Onofri, M., and Martelli, E., "Role of Wall Shape on the Transition in Dual-Bell Nozzles," *Journal of Propulsion and Power*, Vol. 21, No. 2, March–April 2005, pp. 243–250. doi:10.2514/1.6524

[15] Immich, H., and Caporicci, M., "Status of the FESTIP Rocket Propulsion Technology Programme," 33rd AIAA/ASME/SAE/ASEE Joint Propulsion Conference, AIAA Paper 97-3311, July 1997.

[16] Nasuti, F., Onofri, M., and Pietropaoli, E., "The Influence of Nozzle Shape on the Shock Structure in Separated Flows," *Proceedings of the 5th European Symposium on Aerothermodynamics for Space Vehicles*, ESA SP-563, European Space Research and Technology Centre, Noordwijk, The Netherlands, 2005.

[17] Nasuti, F., and Onofri, M., "Analysis of Unsteady Supersonic Viscous Flows by a Shock Fitting Technique," *AIAA Journal*, Vol. 34, No. 7, July 1996, pp. 1428–1434; also AIAA Paper 95-2159.

[18] Nasuti, F., "A Multi-Block Shock-Fitting Technique to Solve Steady and Unsteady Compressible Flows," *Computational Fluid Dynamics 2002*, edited by S. Armeld, P. Morgan, and K. Srinivas, Springer–Verlag, Berlin, 2003, pp. 217–222.

[19] Moretti, G., "A Technique for Integrating Two-Dimensional Euler Equations," *Computers and Fluids*, Vol. 15, No. 1, 1987, pp. 59–75. doi:10.1016/0045-7930(87)90005-3

[20] Paciorri, R., "Sviluppo di una Metodologia Numerica in Forma Quasi-Lineare e Analisi di Modelli Termochimici per lo Studio di Flussi Viscosi Ipersonici," Ph.D. Thesis, Univ. of Rome "La Sapienza," Rome, Feb. 1995.

[21] Paciorri, R., and Sabetta, F., "Compressibility Correction for the Spalart–Allmaras Model in Free-Shear Flows," *Journal of Spacecraft and Rockets*, Vol. 40, No. 3, May 2003, pp. 326–331. doi:10.2514/2.3967

[22] Spalart, P. R., and Allmaras, S. R., "A One-Equation Turbulence Model for Aerodynamic Flows," *La Recherche Aerospatiale*, No. 1, 1994, pp. 5–21.

[23] Bogdanoff, D. W., "Compressibility Effects in Turbulent Shear Layer," *AIAA Journal*, Vol. 21, No. 6, June 1983, pp. 926–927. doi:10.2514/3.60135

[24] Papamoschou, D., and Roshko, A., "The Compressible Turbulent Shear Layer: An Experimental Study," *Journal of Fluid Mechanics*, Vol. 197, Dec. 1988, pp. 453–477. doi:10.1017/S0022112088003325

[25] Nguyen, A., Deniau, H., Girard, S., and de Roquefort, T. A., "Unsteadiness of Flow Separation and End-Effects Regime in a Thrust-Optimized Contour Rocket Nozzle," *Flow, Turbulence and Combustion*, Vol. 71, Nos. 1–4, March 2003, pp. 161–181. doi:10.1023/B:APPL.0000014927.61427.ad

[26] Deck, S., and Nguyen, A., "Unsteady Side Loads in a Thrust-Optimized

Contour Nozzle at Hysteresis Regime," *AIAA Journal*, Vol. 42, No. 9, Sept. 2004, pp. 1878–1888.
doi:10.2514/1.2425

[27] Wang, T.-S., "Transient Three-Dimensional Analysis of Side Load in Liquid Rocket Engine Nozzles," AIAA Paper 2004-3681, July 2004.

[28] Shimizu, T., Miyajima, H., and Kodera, M., "Numerical Study of Restricted Shock Separation in a Compressed Truncated Perfect Nozzle," *AIAA Journal*, Vol. 44, No. 3, March 2006, pp. 576–584.
doi:10.2514/1.14288

[29] Schmucker, R. H., "Flow Process in Overexpanded Chemical Rocket Nozzles. Part 2: Side Loads due to Asymmetric Separation," NASA TM-77395, Feb. 1984.

[30] Schmucker, R. H., "Flow Process in Overexpanded Chemical Rocket Nozzles. Part 1: Flow Separation," NASA TM-77396, Jan. 1984.

[31] Reijasse, P., and Boccaletto, L., "Nozzle Flow Control with a Wall Film Injection," 43rd AIAA/ASME/SAE/ASEE Joint Propulsion Conference, AIAA Paper 07-5747, July 2007.

J. Gore
*Associate Editor*